water

MDPI

*Article*

# Large-Eddy Simulation of the Effects of Frame Tapering on Flow and Turbulence Around Open-Frame Artificial Reefs

**Junfeng Shi [1], Qinghua Xiao [2], Dongdong Guo [3], Yang Lu [4,*], Zhiyuan Dai [5], Xiang Liang [6] and Lu Gao [4,7]**

[1] Hydraulic Engineering Department, Nanjing Hydraulic Research Institute, Nanjing 210029, China; nhrishi@163.com
[2] Changjiang Institute of Survey, Design and Research, Wuhan 430010, China; xiaoqinghua@cjwsjy.com.cn
[3] Yunhe (Henan) Information Technology Co., Ltd., Zhengzhou 450003, China; guodongdong@yrec.cn
[4] Department of River and Harbor Engineering, Nanjing Hydraulic Research Institute, Nanjing 210024, China; gaolu1017@outlook.com
[5] College of Water Conservancy and Hydropower Engineering, Hohai University, Nanjing 210024, China; 241602010023@hhu.edu.cn
[6] Nantong Water Conservancy Survey and Design Institute Co., Ltd., Nantong 226000, China; lx0929231x@163.com
[7] Haikou Marine Center, Ministry of Natural Resources, Haikou 570100, China
* Correspondence: luyang@nhri.cn

## Abstract

The geometry of artificial reefs (ARs) plays an important role in determining their hydrodynamic characteristics, yet the effects of side-frame inclination on flow separation and wake turbulence have received limited attention. This study combines laboratory measurements and three-dimensional large-eddy simulations (LESs) to investigate four open-frame AR configurations with side-frame slope angles of $\theta = 90°, 85°, 80°$, and $75°$. All configurations retain the same overall dimensions and frame topology, with approximately equal solid volumes to minimise differences associated with structural material volume. The LES predictions show good agreement with experiments. Decreasing the slope angle substantially modifies the mean wake structure, with the upper recirculation region of A75 becoming approximately 2.8 times longer and 2.5 times thicker than that of A90, while the lower recirculation region exhibits more moderate changes. Frame tapering also alters the spatial distribution of turbulent kinetic energy, with more pronounced localised high-TKE regions near the upper separated shear layer and a greater concentration of instantaneous vortical structures within the main wake. All tapered configurations produce larger upwelling volumes than A90, with A75 exhibiting the largest increase of approximately 9.3%. In contrast, the wake volume, defined by negative time-averaged streamwise velocity, decreases with decreasing slope angle, reaching a reduction of approximately 13.4% for A75. These findings highlight side-frame inclination as an important geometric parameter for regulating the hydrodynamic characteristics of open-frame artificial reefs.

**Keywords:** artificial reef; large-eddy simulation; flow separation; coherent structures; upwelling region; wake region

Check for updates

Academic Editor: Paolo Mignosa

Received: 10 October 2026
Revised: 3 November 2026
Accepted: 4 November 2026
Published: 6 November 2026

**Copyright:** © 2026 by the authors. Licensee MDPI, Basel, Switzerland. This article is an open access article distributed under the terms and conditions of the Creative Commons Attribution (CC BY) license.

## 1. Introduction

Artificial reefs (ARs) and related artificial habitat structures are widely used in marine and riverine environments for habitat enhancement, fisheries management, and the restoration of degraded aquatic ecosystems [1–4]. In addition to providing physical shelter and increasing habitat complexity, these structures offer refuge, resting, spawning, and feeding

habitats for aquatic organisms [5,6]. ARs also substantially modify the surrounding flow field. As the approaching current encounters a reef, part of the flow is redirected upward and around the structure, while low-velocity and recirculating regions develop within and downstream of it [7,8]. This redistribution of flow can enhance local water exchange and promote the transport of suspended material and nutrients [9,10]. The low-velocity wake also provides hydraulically sheltered areas that may benefit aquatic organisms [5,7]. In open-frame reefs, flow separation from individual frame members and interactions between streams passing through the openings give rise to complex three-dimensional turbulent structures [11,12]. Therefore, understanding how reef geometry influences the surrounding flow field is essential for evaluating the hydrodynamic performance of ARs and guiding their design and deployment.

The upwelling and wake regions are two characteristic flow regions commonly used to evaluate the hydrodynamic performance of artificial reefs (ARs) [7,8]. Their dimensions and spatial distributions are closely related to water exchange, low-velocity sheltering, and the overall hydrodynamic response of reef structures. Previous studies have shown that these regions are strongly influenced by reef geometry and deployment conditions. Kim et al. [7] numerically investigated 24 representative AR types and found considerable differences in wake length among different structural configurations, highlighting the influence of reef geometry on wake development. For permeable reefs, openings provide pathways for water exchange and modify the flow both within and downstream of the structure. Zheng et al. [11] examined the flow around perforated box-type reefs and identified complex turbulent flow characteristics associated with the internal openings and downstream wake. In addition to structural geometry, reef arrangement plays an important role in determining the surrounding flow field. Liu and Su [13] investigated the hydrodynamic interactions between neighbouring reef units and showed that variations in spacing and arrangement affect flow interference and the extent of downstream low-velocity regions. The influence of overall reef shape has also received increasing attention. Maslov et al. [14] compared multifunctional reefs with circular and droplet-shaped cross-sections and reported substantial differences in the volumes of the upwelling and wake regions. Zhou et al. [15] further examined trapezoidal ARs and demonstrated that the angle of attack and opening ratio significantly affect the development of these regions. Collectively, these studies highlight the importance of reef geometry in controlling upwelling and wake characteristics and provide a basis for further optimisation of artificial-reef configurations.

The flow around artificial reefs is complex three-dimensional and highly turbulent, involving complex interactions between the approaching current, structural members, and the developing wake. These characteristics make numerical modelling an important tool for investigating reef hydrodynamics, as it provides detailed flow information that is difficult to obtain solely from laboratory experiments or field measurements. Many previous studies have employed Reynolds-averaged Navier–Stokes (RANS) models, particularly the $k$–$\varepsilon$ and $k$–$\omega$ models, to predict the time-averaged flow field and evaluate the upwelling and wake characteristics of artificial reefs [16,17]. Although these approaches are useful for assessing mean flow patterns, conventional RANS models do not directly resolve the instantaneous turbulent structures associated with shear-layer instability and vortex shedding. Large-eddy simulation (LES), in contrast, resolves the energy-containing turbulent motions while modelling the smaller subgrid scales, providing access to both time-averaged flow statistics and instantaneous three-dimensional vortical structures [18–22]. Despite its advantages, LES has been applied less extensively to artificial reefs than RANS-based approaches. Dai et al. [12] investigated the effects of inflow angle on the hydrodynamics and turbulent structures around a cuboid artificial reef using LES, revealing substantial changes in flow separation and vortex organisation. Leftheriotis et al. [23] further examined turbulent

oscillatory flow around an artificial reef and characterised the development of turbulence within and downstream of the structure. These studies demonstrate the potential of LES for investigating the complex flow processes associated with artificial-reef geometries.

Despite extensive studies on artificial-reef geometry, relatively little attention has been paid to how variations in side-frame inclination influence the surrounding flow field. Previous investigations have considered the effects of opening ratio, angle of attack, overall reef shape, and deployment arrangement on the upwelling and wake characteristics of artificial reefs [14,15]. However, variations in side-frame inclination may also alter the location of flow separation, the development of shear layers, and the structure of the downstream wake. Their influence on mean recirculation patterns, turbulence distribution, and instantaneous three-dimensional vortical structures remains insufficiently understood. Moreover, comparisons between different reef geometries often involve changes in both structural dimensions and solid volume, making it difficult to distinguish the effects of frame tapering from those of other geometric variations. A systematic investigation of different side-frame slope angles, while maintaining consistent overall dimensions, frame topology, and approximately equal solid volumes, is therefore needed to better understand the associated hydrodynamic responses.

The present study combines laboratory experiments and three-dimensional large-eddy simulation (LES) to investigate the effects of frame tapering on the flow characteristics and turbulent structures of open-frame artificial reefs. The paper is organised as follows: Section 2 describes the experimental setup, numerical methods, computational configuration, and model validation. Section 3 examines the time-averaged and instantaneous flow characteristics, turbulence distributions, and upwelling and wake regions. Section 4 summarises the main conclusions.

## 2. Laboratory Experiments and Numerical Simulations

### 2.1. Laboratory Setup

The experiments were conducted in a rectangular flume at the Hydraulics Laboratory of Hohai University. The flume was 8.0 m long, 0.5 m wide, and 0.5 m high. Water was supplied through a recirculating system, and a flow straightener was installed near the flume inlet to reduce incoming disturbances and provide a nearly uniform approaching flow. The water depth was maintained at $H = 0.40$ m, with a bulk approaching velocity of $U_b = 0.10$ m/s. The artificial reef (AR) model was fixed to the flume bed, with its centre located 5.0 m downstream of the inlet [Figure 1a]. As illustrated in Figure 1b, the experimental model corresponded to the reference configuration A90, featuring a cubic open-frame structure with vertical side frames ($\theta = 90°$). The model was fabricated from acrylic, with an external side length of $D = 0.10$ m. Each face contained a centred square opening with a clear width of 0.07 m, corresponding to a frame-member width of 0.015 m.

Instantaneous velocities were measured using an acoustic Doppler velocimeter (ADV) (SonTek, San Diego, CA, USA) at a sampling frequency of 50 Hz. Data were recorded continuously for 180 s at each sampling location, yielding 9000 instantaneous velocity samples per point. Measurements were taken along two lines in the longitudinal vertical plane passing through the centre of the AR [Figure 1c]. Line $L_1$ was aligned with the streamwise direction at 0.05 m above the top of the AR, while Line $L_2$ extended vertically at 0.08 m downstream of its rear face. The resulting velocity profiles were used to validate the LES predictions.

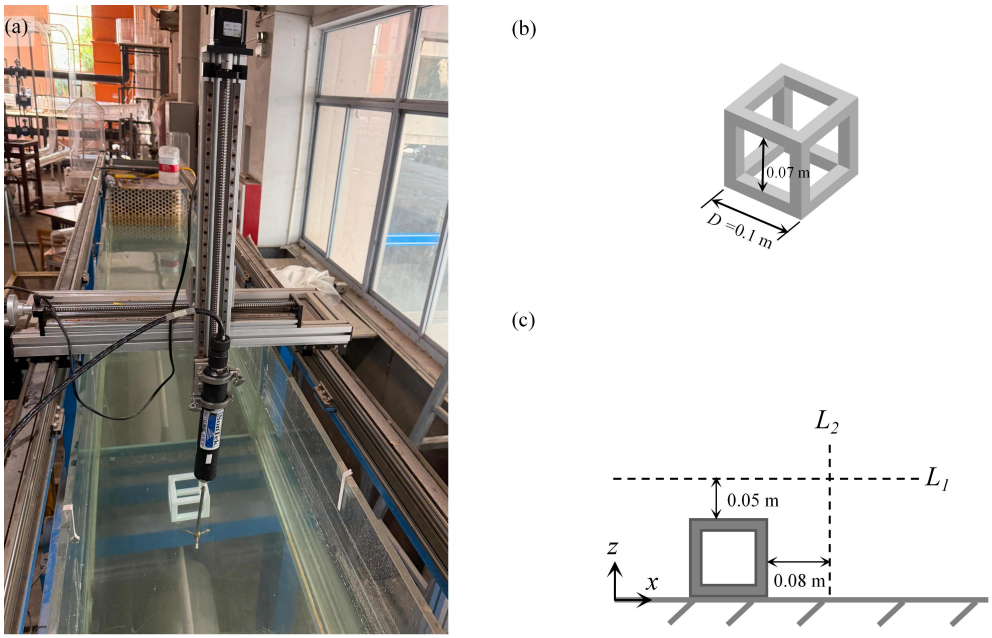



**Figure 1.** Experimental setup and measurement locations: (**a**) laboratory flume and ADV measurement system; (**b**) geometry of the reference artificial reef configuration (A90); and (**c**) locations of the velocity measurement lines $L_1$ and $L_2$.

### *2.2. Numerical Framework*

Three-dimensional large-eddy simulations (LESs) were performed using WaterLily.jl v1.7.0, an open-source finite-volume solver for incompressible viscous flows [24]. The spatially filtered continuity and momentum equations are given by

$$\frac{\partial \overline{u}_i}{\partial x_i} = 0, \tag{1}$$

and

$$\frac{\partial \overline{u}_i}{\partial t} + \frac{\partial (\overline{u}_i \overline{u}_j)}{\partial x_j} = -\frac{\partial \overline{p}}{\partial x_i} + \nu \frac{\partial^2 \overline{u}_i}{\partial x_j \partial x_j} - \frac{\partial \tau_{ij}}{\partial x_j}, \tag{2}$$

where $\overline{u}_i$ denotes the resolved velocity component, $\overline{p}$ is the filtered pressure normalised by the constant fluid density $\rho$, and $\nu$ is the kinematic viscosity. Repeated indices imply summation over the three Cartesian directions. The subgrid-scale (SGS) stress tensor is defined as

$$\tau_{ij} = \overline{u_i u_j} - \overline{u}_i \overline{u}_j. \tag{3}$$

The unresolved stresses are modelled using the Smagorinsky–Lilly eddy-viscosity model [25,26],

$$\tau_{ij} - \frac{1}{3}\tau_{kk}\delta_{ij} = -2\nu_t \overline{S}_{ij}, \qquad \nu_t = (C_s \Delta)^2 \left(2\overline{S}_{mn}\overline{S}_{mn}\right)^{1/2}, \tag{4}$$

where the resolved strain-rate tensor is

$$\overline{S}_{ij} = \frac{1}{2}\left(\frac{\partial \overline{u}_i}{\partial x_j} + \frac{\partial \overline{u}_j}{\partial x_i}\right), \tag{5}$$

and $\delta_{ij}$ is the Kronecker delta. The Smagorinsky coefficient was fixed at $C_s = 0.17$, consistent with previous LES studies [27,28]. The filter width was defined as

$$\Delta = (\Delta x \Delta y \Delta z)^{1/3}, \tag{6}$$

which reduces to the local grid spacing for the uniform isotropic mesh adopted in the present simulations. The isotropic SGS contribution was incorporated into the modified pressure,

$$p^{\dagger} = \overline{p} + \frac{1}{3}\tau_{kk}. \tag{7}$$

The governing equations were discretised on a Cartesian staggered grid, with pressure stored at cell centres and velocity components located at cell faces. Second-order central differences were employed for the pressure-gradient and viscous terms, whereas the convective fluxes were evaluated using a flux-limited QUICK scheme [24,29]. The SGS viscosity was updated from the resolved velocity gradients during each stage of the time integration.

The artificial reef geometry was imported as a triangulated STL surface and represented using WaterLilyMeshBodies.jl v0.1.3. The solid boundary was incorporated through the boundary data immersion method (BDIM) [30,31]. In this approach, the fluid and solid momentum equations are blended smoothly across the immersed interface using a regularised convolution kernel. The zeroth- and first-order kernel moments account for the velocity transition and the variation normal to the interface, respectively. Retaining the first-order moment correction provides second-order accuracy in the treatment of the immersed boundary [31]. Because the AR remained stationary throughout the simulations, the prescribed solid velocity was set to zero, thereby imposing a no-slip condition on its surface.

Time advancement was carried out using a second-order explicit predictor–corrector scheme. At each stage, a pressure-projection procedure was applied to enforce discrete incompressibility, leading to a variable-coefficient Poisson equation that accounts for the immersed-boundary formulation. The pressure equation was solved using a geometric multigrid method. The time step was adjusted automatically according to the solver stability criterion. All simulations were executed on an NVIDIA GPU through the CUDA backend of WaterLily.jl.

### *2.3. Computational Setups and Boundary Conditions*

The numerical simulations were conducted under the same inflow velocity and water-depth conditions as the laboratory experiments. Figure 2a illustrates the computational domain, which extended $20D$, $8D$, and $4D$ in the streamwise ($x$), spanwise ($y$), and vertical ($z$) directions, respectively, where $D = 0.10$ m is the characteristic length of the AR. The AR was centred at $x = 6D$, providing upstream and downstream domain lengths of $6D$ and $14D$, respectively, relative to the reef centre. The water depth was maintained at $H = 4D = 0.40$ m, consistent with the experimental conditions. A wider computational domain ($8D$) than the experimental flume ($5D$) was adopted to reduce lateral confinement and minimise sidewall effects on the flow around the AR.

A uniform streamwise velocity of $U_b = 0.10$ m/s was prescribed at the inlet, while a convective boundary condition was applied at the outlet to allow flow disturbances to leave the domain with minimal numerical reflection. With a uniform inlet velocity and an upstream distance of $6D$, the approach flow remains in a developing state before reaching the AR. No-slip boundary conditions were imposed on the bed and sidewalls, whereas a free-slip condition was applied at the upper boundary. The latter was treated using a rigid-lid approximation, as the depth-based Froude number was approximately 0.05 ($Fr = U_b/\sqrt{gH}$, where $g$ is the gravitational acceleration), indicating negligible free-surface deformation under the present flow conditions [32,33]. To improve the resolution of flow separation and near-wake structures, local mesh refinement was introduced within $0.4\text{ m} < x < 1.2\text{ m}$, $-0.2\text{ m} < y < 0.2\text{ m}$, and $0 < z < 0.3$ m, as indicated in Figure 2a. The refined region encompassed the entire AR and extended approximately $6D$ downstream

of its centre. Within this region, the grid spacing was reduced by a factor of two in each coordinate direction relative to the background mesh, providing enhanced spatial resolution near the AR without applying the finest grid throughout the computational domain.

Four AR configurations were considered to investigate the effects of frame tapering on the surrounding flow. The side-frame slope angles were $\theta = 90°$, 85°, 80°, and 75°, corresponding to configurations A90, A85, A80, and A75, respectively [Figure 2b]. As illustrated in Figure 2c, $\theta$ denotes the angle between the inclined side frame and the horizontal base. All configurations retained the same base width $D$, overall height $D$, frame-member width of 0.015 m, and frame topology. As $\theta$ decreased, the side frames became increasingly inclined towards the reef centre, resulting in a progressive reduction in the top width $D_t$. For the cubic configuration A90, the solid volume was calculated as $V_s = 12Db^2 - 16b^3 = 0.216D^3$, where $b = 0.015$ m denotes the square cross-sectional width of the frame members. For the remaining configurations, the solid volume varied with the frame geometry as the slope angle decreased.

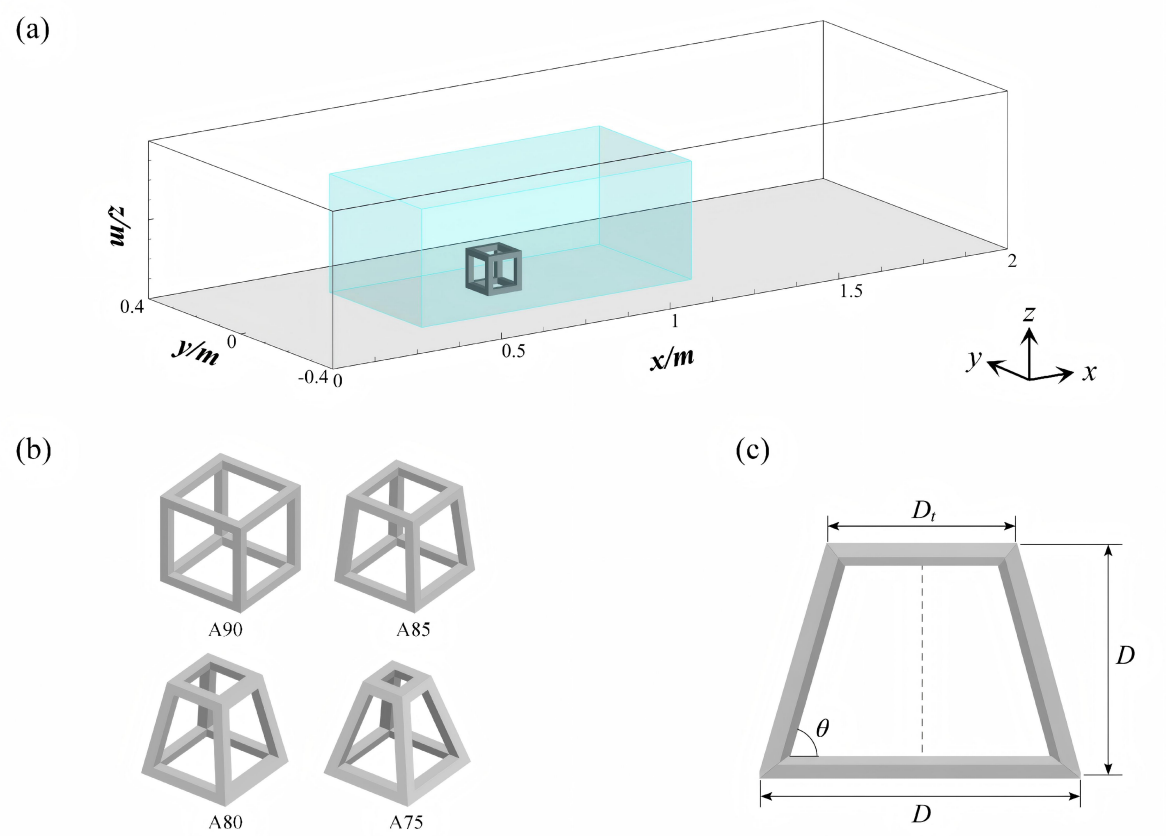



**Figure 2.** Computational domain and artificial-reef configurations: (**a**) computational domain and locally refined region; (**b**) four AR configurations with side-frame slope angles of $\theta = 90°$, 85°, 80°, and 75° (A90–A75); and (**c**) definition of the geometric parameters $D$, $D_t$, and $\theta$.

Two mesh resolutions were examined to assess the sensitivity of the numerical results to grid refinement. Both meshes employed the same local-refinement strategy, with the grid spacing in the refined region reduced by a factor of two relative to the background mesh. The corresponding grid spacings are summarised in Table 1. For Mesh 1, the background and refined grid spacings were 0.004 m and 0.002 m, respectively. These values were halved for Mesh 2, resulting in grid spacings of 0.002 m and 0.001 m. Isotropic cells were employed at both resolution levels, with $\Delta x = \Delta y = \Delta z$ within each region.

**Table 1.** Grid spacings adopted for the mesh-sensitivity analysis.

| Mesh | Background Region $\Delta x = \Delta y = \Delta z$ (m) | Refined Region $\Delta x = \Delta y = \Delta z$ (m) |
|---|---|---|
| Mesh 1 | 0.004 | 0.002 |
| Mesh 2 | 0.002 | 0.001 |

The numerical predictions obtained with the two meshes were compared with the acoustic Doppler velocimeter (ADV) measurements along Lines $L_1$ and $L_2$ shown in Figure 1c. Figure 3 presents the normalised time-averaged streamwise velocity, $U_m/U_b$, and turbulent kinetic energy, $TKE/U_b^2$. Here, $U_m = \overline{u}$ denotes the temporal mean of the instantaneous streamwise velocity $u$, and $U_b$ is the bulk approaching velocity. Experimental measurements are shown as symbols, while dashed and solid lines represent the predictions from Mesh 1 and Mesh 2, respectively.

Along the streamwise measurement line $L_1$ [Figure 3a], $U_m/U_b$ remains close to unity in the upstream portion of the profile before increasing to a peak of approximately 1.11. The velocity subsequently decreases downstream, approaching values of approximately 1.03–1.05 towards the end of the measurement line. Both meshes reproduce this acceleration and the subsequent velocity reduction, with Mesh 2 providing slightly better agreement near the peak. A more pronounced velocity variation is observed along the vertical measurement line $L_2$ [Figure 3b]. The streamwise velocity initially increases with distance from the bed, followed by a marked reduction within the AR wake. The minimum value of $U_m/U_b$ is approximately 0.6 and occurs near the mid-height of the wake. Above this region, the velocity recovers and slightly exceeds the approaching-flow velocity. Both meshes capture the principal features of the vertical profile, including the wake-induced velocity deficit and subsequent recovery. The largest discrepancies between the numerical and experimental results occur near the bed, while the agreement elsewhere is generally good.

The corresponding TKE distributions are presented in Figure 3c,d. Along $L_1$, TKE remains low over most of the profile before increasing markedly further downstream. Both meshes capture this trend, although Mesh 2 predicts slightly higher TKE in the downstream region. Along $L_2$, the TKE distribution exhibits two local peaks, with Mesh 2 generally predicting higher peak values than Mesh 1. Overall, both meshes reproduce the main spatial variations in TKE, while Mesh 2 shows closer agreement with the experimental measurements in the regions of elevated turbulence.

The differences between Mesh 1 and Mesh 2 are relatively small for the mean velocity profiles, while some differences are observed in the predicted TKE peaks. Grid refinement produces only minor changes in the principal velocity extrema and their locations, and both meshes reproduce the main spatial variations in TKE. Mesh 2 generally provides closer agreement with the experimental measurements, particularly in regions of strong velocity gradients and elevated turbulence. Accordingly, Mesh 2 was adopted for the subsequent simulations.

The near-wall resolution of Mesh 2 was further assessed using the dimensionless wall-normal distance, $\Delta\eta^+$. As summarised in Table 1, an isotropic grid spacing of $\Delta x = \Delta y = \Delta z = 0.001$ m was employed within the locally refined region. The dimensionless wall-normal distance was calculated at fluid sampling locations adjacent to the solid boundaries as [21,34]

$$\Delta\eta^+ = \frac{\Delta\eta u_\tau}{\nu}, \tag{8}$$

where $\Delta\eta$ is the wall-normal distance from the solid surface to the adjacent fluid sampling point, $u_\tau$ is the local friction velocity, and $\nu$ is the kinematic viscosity. Assuming a locally linear tangential velocity profile near the wall, the friction velocity was approximated by

$$u_\tau \approx \left(\frac{\nu U_t}{\Delta\eta}\right)^{1/2}, \tag{9}$$

where $U_t$ denotes the magnitude of the local time-averaged tangential velocity at the sampling point.

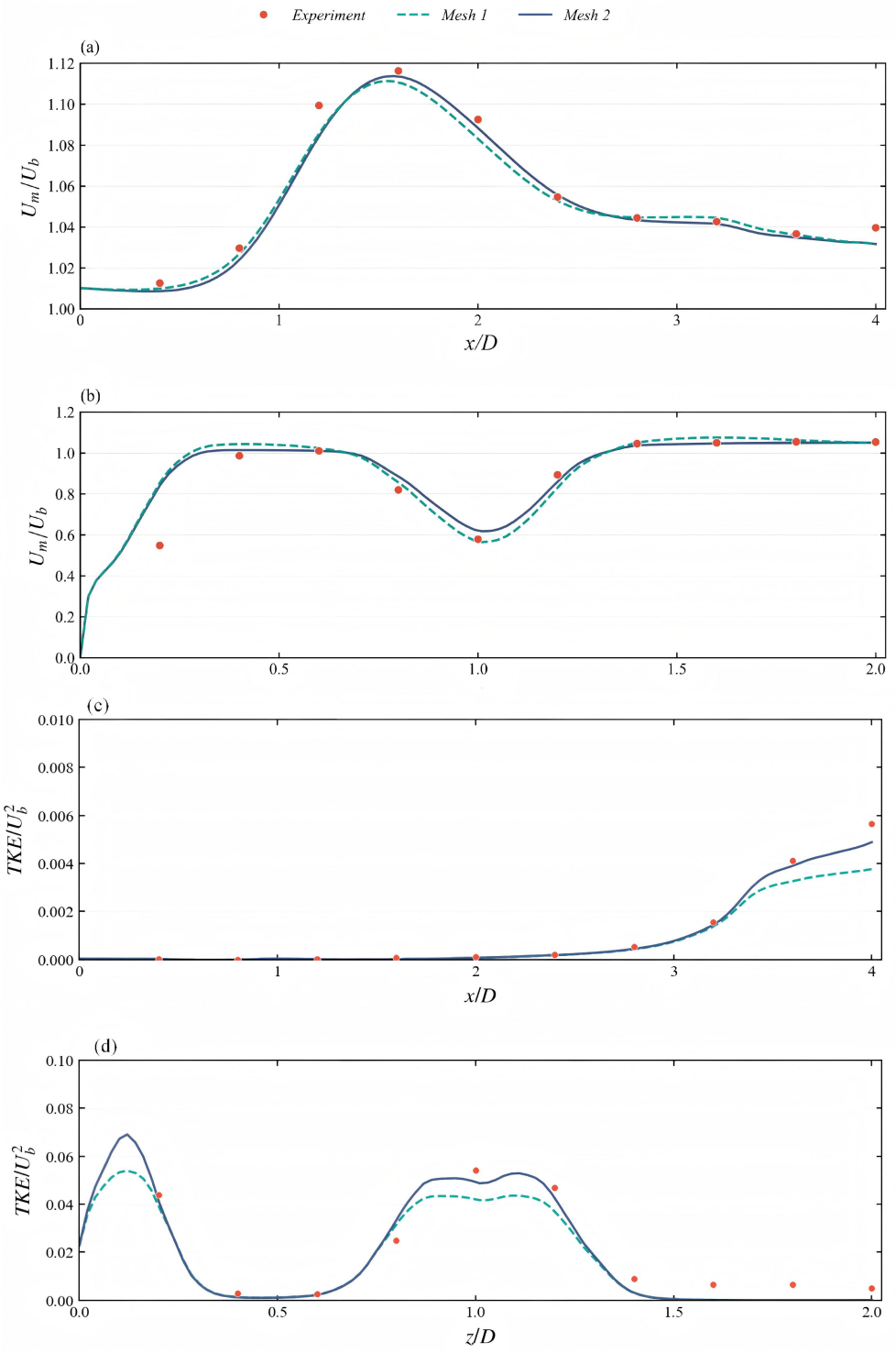



**Figure 3.** Comparison of normalised time-averaged streamwise velocity and turbulent kinetic energy (TKE) profiles obtained from ADV measurements and LES predictions using Mesh 1 and Mesh 2: (**a**) streamwise velocity along Line $L_1$; (**b**) streamwise velocity along Line $L_2$; (**c**) TKE along Line $L_1$; and (**d**) TKE along Line $L_2$.

Figure 4 shows the distribution of $\Delta\eta^+$ over the AR surfaces and the flume bed within the locally refined region. The values remain below approximately 5 over most of the solid surfaces, indicating that the near-wall sampling points are predominantly located within or close to the viscous sublayer [35,36]. Locally elevated values occur around the upstream-facing edges and corners of the AR frame, where the flow encounters the structural members and relatively large near-wall velocity gradients develop. Lower values are generally observed over sheltered surfaces and in the downstream region, consistent with the reduced local tangential velocities and wall shear.

The generally low values of $\Delta\eta^+$ suggest that Mesh 2 provides a reasonably fine near-wall resolution for the present simulations. Together with the limited sensitivity of the time-averaged velocity profiles to grid refinement and their agreement with the ADV measurements in Figure 3, these results support the selection of Mesh 2 for the subsequent analysis of the flow around the four AR configurations.

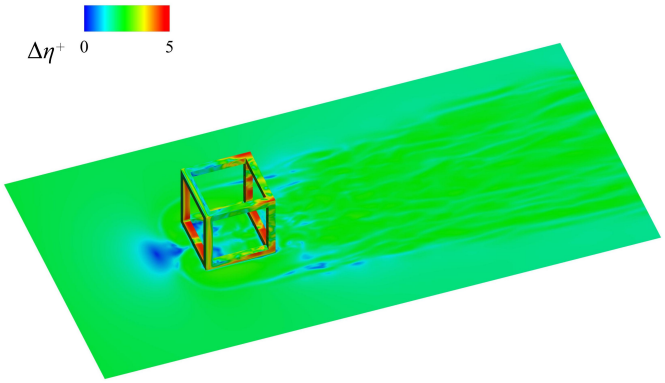



**Figure 4.** Distribution of the dimensionless wall-normal distance, $\Delta\eta^+$, over the artificial reef surfaces and the flume bed within the locally refined region for Mesh 2.

## 3. Results and Discussions

### *3.1. Time-Averaged Flow Field and Flow Separation*

Figure 5 presents the distributions of the normalised time-averaged streamwise velocity, $U_m/U_b$, for the four AR configurations. Figure 5a–d show the horizontal distributions at the mid-height of the AR, while Figure 5e–h present the corresponding longitudinal vertical sections through the reef centre. Enlarged views of the near-wake region, with streamlines superimposed, are provided in Figure 5i–l. In the horizontal plane, all configurations exhibit a pronounced velocity deficit downstream of the AR. For A90 [Figure 5a], two distinct low-velocity regions develop behind the lateral frame members, separated by a region of relatively higher streamwise velocity near the wake centreline. A similar pattern is observed for A85, although the low-velocity regions begin to spread and interact farther downstream. As the slope angle decreases to 80° and 75°, these regions become less clearly separated, producing a more continuous low-momentum wake. The longitudinal vertical sections reveal further changes in the flow structure. As the approaching current passes over the AR, the flow accelerates above the upper frame, while a substantial velocity deficit develops immediately downstream of the structure. Two distinct regions of reversed mean streamwise flow are identified: one behind the upper frame and another near the bed. These regions correspond to separate mean recirculation zones associated with flow separation from the upper and lower portions of the AR.

To quantify the recirculation zones, streamlines were generated in Tecplot using the time-averaged streamwise ($U_m$) and vertical ($W_m$) velocity components. The upper and lower recirculation zones were identified based on their locations and recirculating streamline patterns. Their streamwise lengths and maximum vertical thicknesses were

estimated from the spatial extents of the corresponding recirculation patterns. The upper recirculation zone develops immediately downstream of the top frame near $z/D \approx 1$, whereas the lower zone forms close to the bed behind the lower frame. The enlarged streamline patterns in Figure 5i–l show that the dimensions of these regions vary with the slope angle. For the upper recirculation zone, the normalised length, $L_{r,u}/D$, increases from approximately 0.14 for A90 to 0.19, 0.22, and 0.39 for A85, A80, and A75, respectively. The corresponding maximum thickness, $H_{r,u}/D$, increases from 0.06 to 0.10, 0.12, and 0.15. Compared with A90, the upper recirculation zone of A75 is therefore approximately 2.8 times longer and 2.5 times thicker, indicating a pronounced sensitivity of the upper separated flow to frame tapering. The lower recirculation zone exhibits a more moderate response. Its normalised length, $L_{r,l}/D$, increases from approximately 0.48 for A90 to 0.53 for A85 and 0.60 for A80, with little further change for A75. Meanwhile, the maximum thickness, $H_{r,l}/D$, remains close to 0.08 for A90 and A85 before increasing to 0.10 and 0.11 for A80 and A75, respectively. Thus, although the lower recirculation zone becomes somewhat longer and thicker as the frame is tapered, its streamwise extent changes little between A80 and A75.

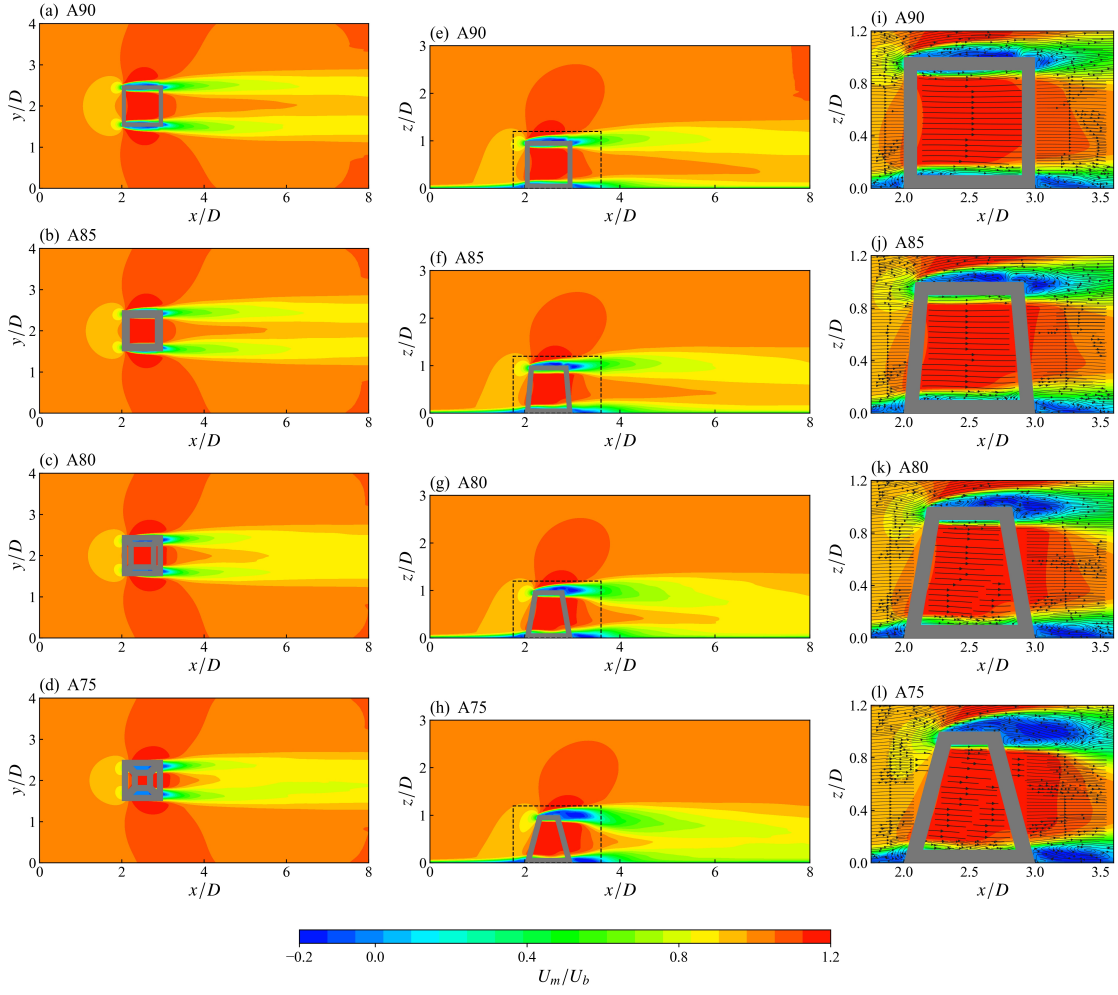



**Figure 5.** Distributions of the normalised time-averaged streamwise velocity, $U_m/U_b$, for the four AR configurations: (**a**–**d**) horizontal sections at the mid-height of the AR for A90, A85, A80, and A75, respectively; (**e**–**h**) corresponding longitudinal vertical sections through the reef centre; and (**i**–**l**) enlarged views of the near-wake region with streamlines superimposed to illustrate the mean recirculation patterns.

Overall, frame tapering modifies the mean wake structure and the spatial distribution of the separated flow behind the AR. The upper recirculation zone responds more strongly

to decreasing slope angle, whereas the lower zone exhibits comparatively limited changes, particularly in its streamwise extent. These differences highlight the distinct responses of the upper and lower separated-flow regions to variations in frame geometry.

### *3.2. Turbulence Characteristics*

The spatial distributions of the normalised turbulent kinetic energy, $TKE/U_b^2$, for the four AR configurations are presented in Figure 6. The turbulent kinetic energy is defined as $TKE = (\overline{u'u'} + \overline{v'v'} + \overline{w'w'})/2$, where $u'$, $v'$, and $w'$ denote the fluctuating velocity components in the streamwise, spanwise, and vertical directions, respectively. Figure 6a–d show the distributions in the horizontal plane at the mid-height of the AR, while Figure 6e–h show the corresponding distributions in the longitudinal vertical plane through the centre of the reef.

In the horizontal plane, elevated TKE is concentrated mainly in two elongated regions extending downstream from the lateral frame members. For A90 [Figure 6a], two distinct high-TKE regions develop immediately behind the side frames and gradually weaken farther downstream. Their locations correspond closely to the separated shear layers bordering the low-velocity wake identified in Figure 5. A similar distribution is observed for A85, although the localised high-TKE regions become more concentrated near the rear of the frame. As the slope angle decreases further, the spatial organisation of turbulence changes appreciably. For A80 and A75 [Figure 6c,d], elevated TKE remains concentrated near the lateral frame members, while the downstream distributions become more closely confined to the main wake region. These differences indicate that frame tapering modifies the development and spatial extent of the turbulent shear layers rather than producing a uniform increase in TKE throughout the wake.

The longitudinal vertical sections further reveal the relationship between the TKE distribution and the mean flow separation around the AR [Figure 6e–h]. Two principal regions of elevated TKE are identified downstream of the structure: an upper region originating near the rear edge of the top frame at $z/D \approx 1$ and a lower region developing close to the bed behind the lower frame. These regions are located along the separated shear layers associated with the upper and lower recirculation zones identified in Figure 5. The elevated TKE is consistent with enhanced turbulent fluctuations across the shear layers, where the outer flow interacts with the low-velocity or reversed flow within the recirculation regions. Farther downstream, TKE generally decreases as the turbulent fluctuations weaken and spread into the surrounding flow.

The influence of frame tapering is particularly evident in the upper portion of the wake. For A90 and A85, the upper high-TKE region extends downstream from the top frame and gradually weakens, whereas A80 and A75 exhibit more pronounced localised TKE concentrations near the upper separated shear layer. Changes are also observed near the bed, although the lower high-TKE region remains relatively confined to the vicinity of the lower frame and its downstream wake. These variations are consistent with the distinct responses of the upper and lower recirculation zones discussed in the preceding section. The correspondence between the mean separation patterns and the TKE distributions suggests that the inclination of the side frames influences not only the geometry of the recirculating flow but also the spatial organisation of turbulent fluctuations in the wake.

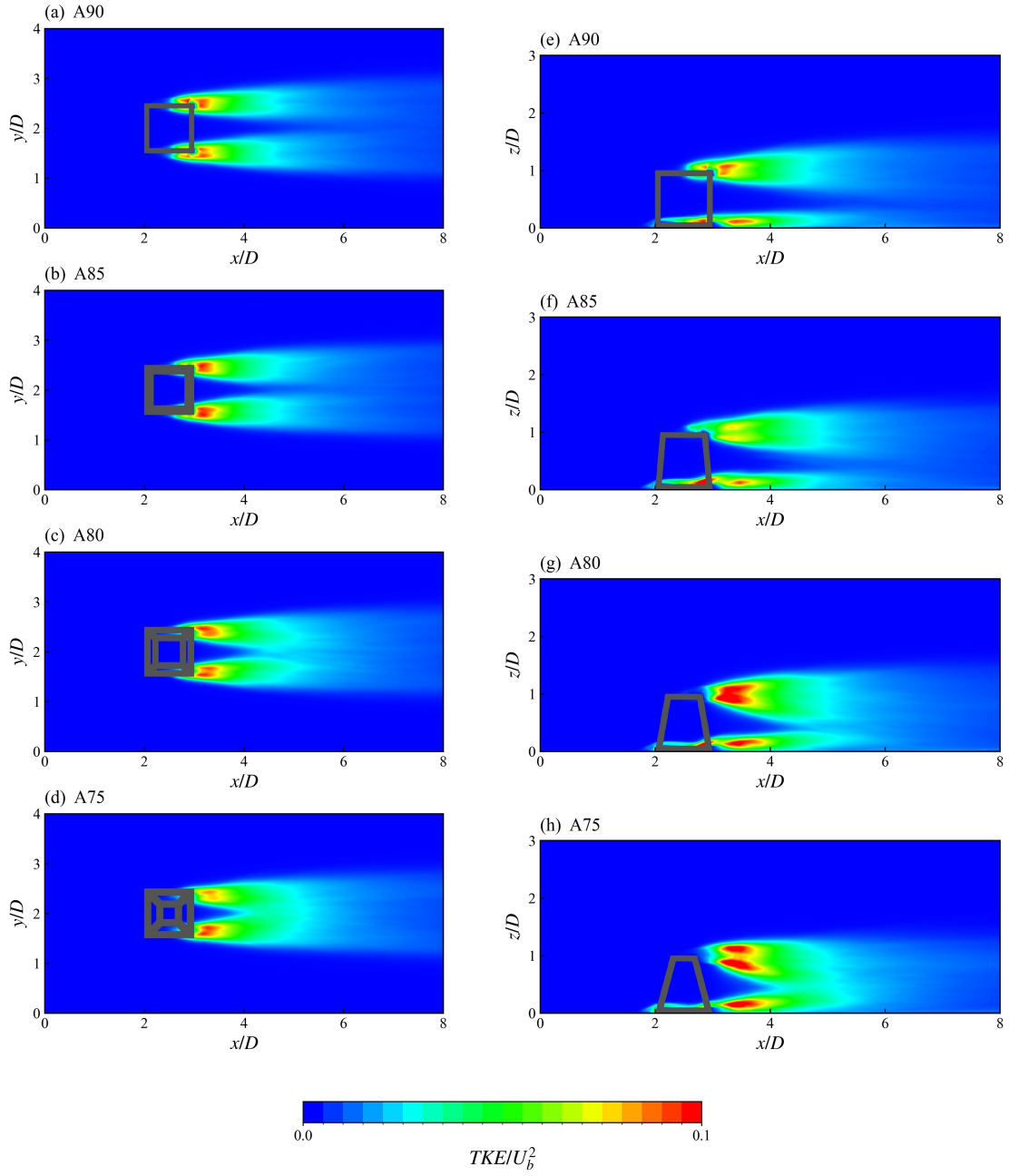



**Figure 6.** Distributions of the normalised turbulent kinetic energy, $TKE/U_b^2$, for the four AR configurations: (**a**–**d**) horizontal sections at the mid-height of the AR for A90, A85, A80, and A75, respectively, and (**e**–**h**) corresponding longitudinal vertical sections through the reef centre.

### *3.3. Instantaneous Flow Structures*

The flow around open-frame artificial reefs is characterised by complex three-dimensional vortical structures arising from flow separation and interactions between the streams passing through the structural openings. The $Q$-criterion, originally proposed by Hunt et al. [37], has been widely used to identify and visualise vortical structures in turbulent flows [38–40]. In the present study, instantaneous vortical structures were visualised using $Q$-criterion isosurfaces at $Q = 50$, coloured by the instantaneous streamwise velocity, $u/U_b$. This threshold was selected to clearly visualise the vortical structures and highlight differences in their spatial distributions among the four AR configurations. Figure 7 presents the results for the four AR configurations, with oblique views shown in Figure 7a–d and the corresponding top views in Figure 7e–h.

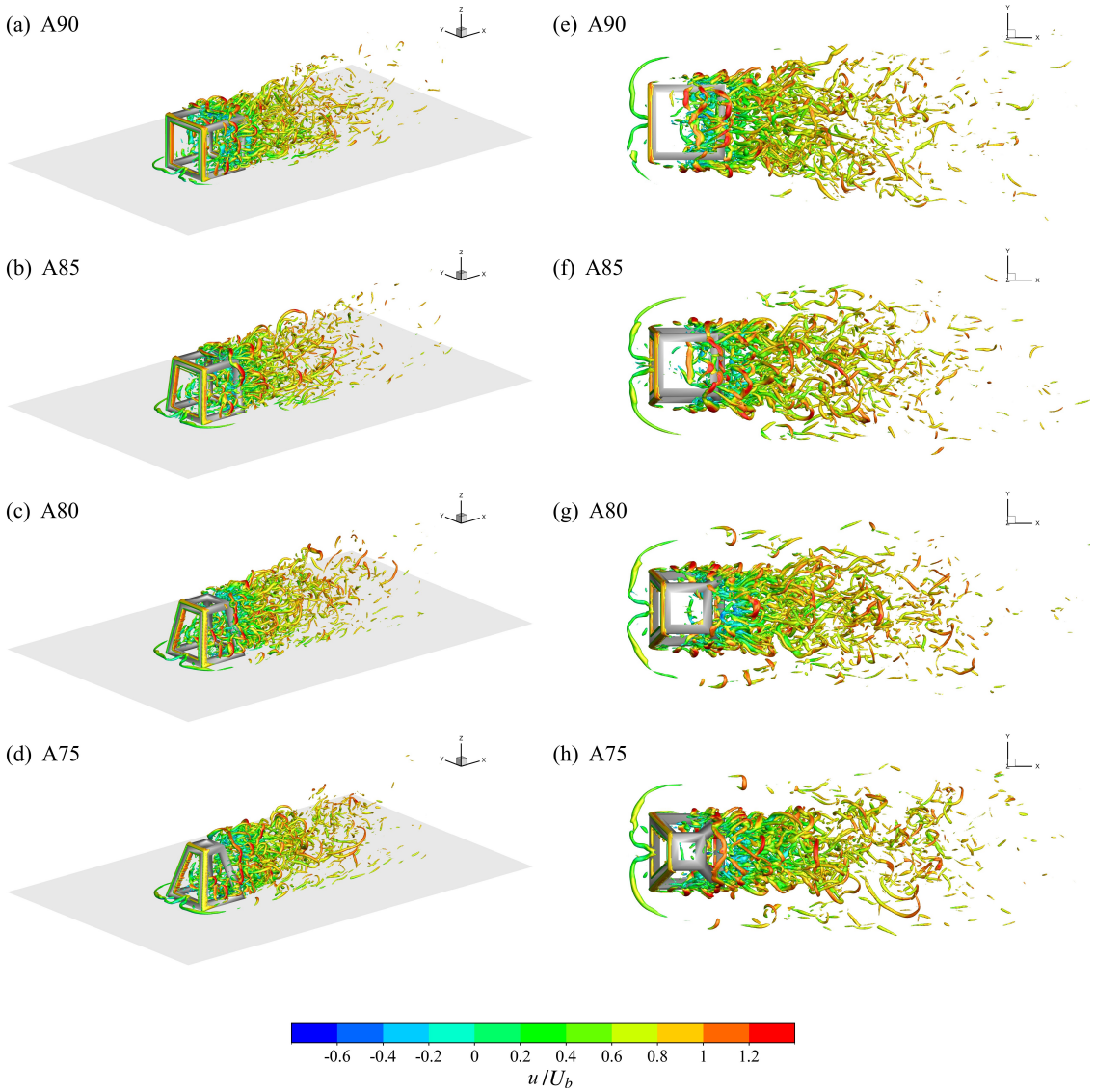



**Figure 7.** Instantaneous vortical structures identified using $Q$-criterion isosurfaces ($Q = 50$) and coloured by the instantaneous streamwise velocity, $u/U_b$, for the four AR configurations: (**a**–**d**) oblique views of A90, A85, A80, and A75, respectively, and (**e**–**h**) corresponding top views.

The oblique views reveal numerous three-dimensional vortical structures concentrated around the frame members and in the immediate wake of the AR. Flow separation at the frame edges and interactions between the streams passing through the internal openings contribute to the formation of these structures. In the near wake, densely distributed vortices exhibit complex shapes and orientations, reflecting interactions among the separated shear layers from different parts of the reef. Farther downstream, the vortical structures become more fragmented and sparsely distributed. The velocity colouring reveals substantial variations in the instantaneous streamwise velocity within the vortex field, including regions of locally reversed flow. These features reflect the complex unsteady motions induced by the open-frame geometry.

The top views provide a clearer comparison of the spanwise distribution of vortical structures among the four configurations. For A90 [Figure 7e], the vortex field extends over a relatively broad lateral region, with numerous structures distributed across the downstream wake. A85 exhibits a broadly similar pattern, although differences in the arrangement and distribution of the vortices are apparent. As the slope angle decreases further, the denser vortical structures become more concentrated within the main wake region.

This tendency is particularly noticeable for A80 and A75 [Figure 7g,h], where relatively fewer isolated structures extend laterally away from the wake. The observed differences suggest that frame tapering modifies the spatial organisation of the instantaneous vortex field, consistent with the changes in mean flow separation and turbulence distribution identified in the preceding sections.

It should be noted that the present analysis was conducted under smooth-bed conditions. In natural marine environments, seabed roughness may modify near-bed velocity distributions, boundary-layer development, and turbulence production. Previous experimental studies of flow around bed-mounted cylinders have reported changes in horseshoe vortex structures and local bed shear stress under rough-bed conditions [41]. Furthermore, LES investigations of flow over boulders on rough, permeable beds have demonstrated complex interactions between near-bed turbulence, separated shear layers, and wake structures [42]. For open-frame ARs, these roughness-induced changes in near-bed flow may affect the interaction between the lower frame and the bed, potentially modifying the development of the lower recirculation region and its associated vortical structures. Further investigations considering different seabed roughness conditions are therefore needed to evaluate these effects and their implications for the hydrodynamic performance of ARs.

### *3.4. Upwelling and Wake Region Characteristics*

To examine the influence of frame tapering on the large-scale flow redistribution around the AR, the volumes of the upwelling and wake regions were evaluated for the four configurations. The upwelling region was defined as the connected flow volume satisfying $W_m/U_b > 0.1$, where $W_m$ denotes the time-averaged vertical velocity [43]. The wake region was defined as the region where the time-averaged streamwise velocity is negative ($U_m < 0$) [8,44]. It should be noted that these volume-based metrics quantify the spatial extent of the upwelling and wake regions but do not account for variations in velocity magnitude within these regions. Figure 8 illustrates the three-dimensional distributions of these regions for A90, A85, A80, and A75, with oblique views shown in Figure 8a–d and corresponding top views in Figure 8e–h.

The oblique views show that the upwelling region develops primarily around the upstream and upper portions of the AR, where the approaching current is diverted upward by the frame. Although its general distribution remains similar among the four configurations, variations in the extent and shape of the upwelling region become apparent as the slope angle decreases. In contrast, the wake region becomes less extensive with increasing frame tapering. The top views further reveal changes in the horizontal distribution of both regions, with the region becoming more confined around the reef as the side frames are progressively inclined.

To quantify these differences, the volumes of both regions were normalised by their corresponding values for A90, as summarised in Table 2. The normalised upwelling volume, $V_{up}/V_{up,A90}$, is 1.0526 for A85 and 1.0419 for A80, increasing to 1.0934 for A75. Although this variation is not monotonic, all tapered configurations exhibit larger upwelling volumes than A90, with the greatest increase of approximately 9.3% occurring for A75. By comparison, the normalised wake volume, $V_{wake}/V_{wake,A90}$, decreases consistently from 1.0000 for A90 to 0.9029, 0.8954, and 0.8662 for A85, A80, and A75, respectively. The reduction is most pronounced for A75, whose wake volume is approximately 13.4% smaller than that of A90.

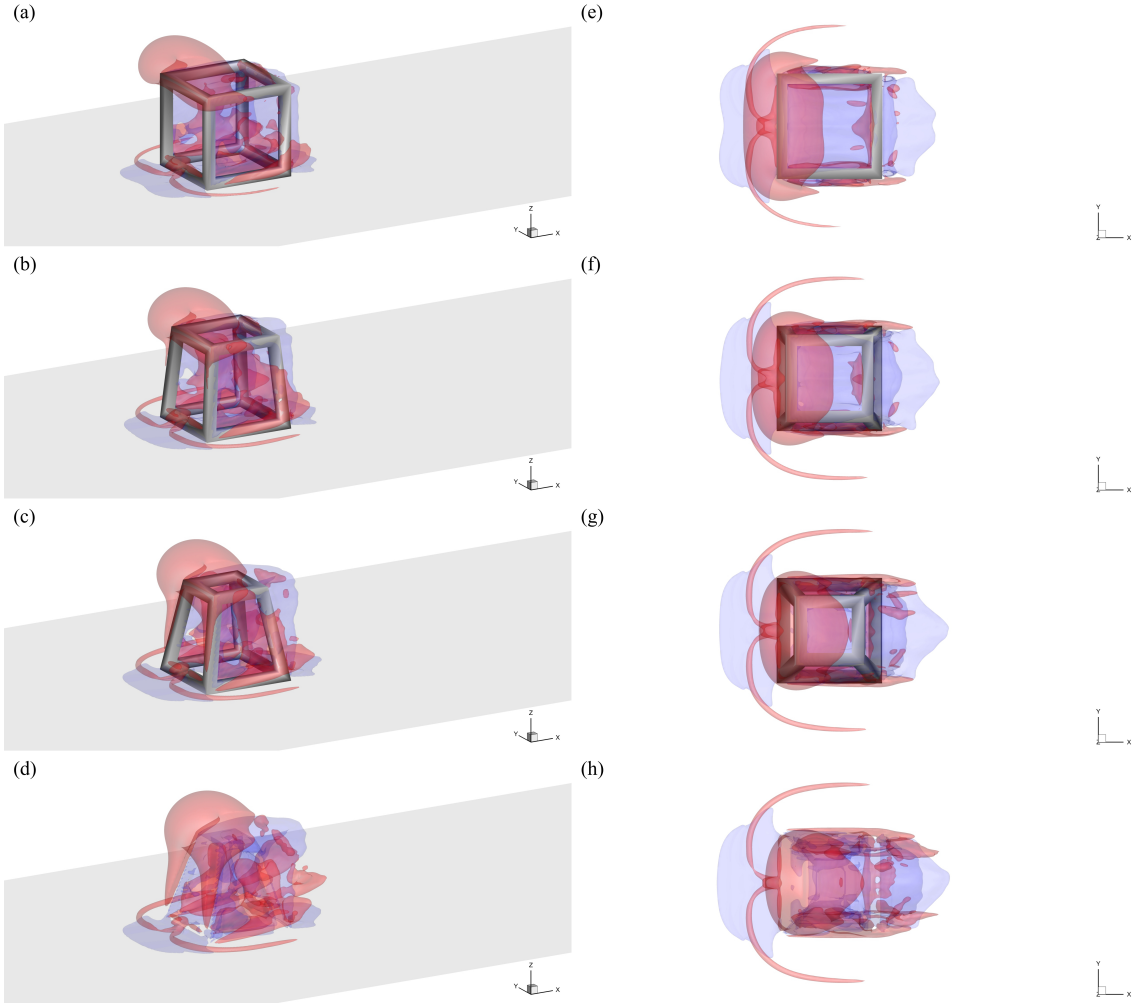



**Figure 8.** Three-dimensional distributions of the upwelling (red) and wake (blue) regions for the four AR configurations, defined by $W_m/U_b > 0.1$ and $U_m/ < 0$, respectively: (**a**–**d**) oblique views of A90, A85, A80, and A75, respectively, and (**e**–**h**) corresponding top views.

**Table 2.** Normalised volumes of the upwelling and wake regions for the four AR configurations. Upwelling volumes are evaluated using three thresholds of $W_m/U_b$, while wake volumes are defined by $U_m < 0$.

| | $V_{up}/V_{up,A90}$ | | | $V_{wake}/V_{wake,A90}$ |
|---|---|---|---|---|
| **Configuration** | **0.05** | **0.10** | **0.15** | $U_m < 0$ |
| A90 | 1.0000 | 1.0000 | 1.0000 | 1.0000 |
| A85 | 0.9454 | 1.0522 | 1.1772 | 0.9029 |
| A80 | 0.9930 | 1.0418 | 1.1596 | 0.8954 |
| A75 | 1.0672 | 1.0932 | 1.1210 | 0.8662 |

The contrasting responses of the upwelling and wake regions indicate that frame tapering alters the redistribution of flow around the AR in different ways. Among the four configurations, A75 produces the largest upwelling volume and the smallest wake volume, highlighting the sensitivity of these hydrodynamic characteristics to the side-frame slope angle.

To evaluate the sensitivity of the upwelling volume to the threshold selection, two additional thresholds of $W_m/U_b > 0.05$ and $W_m/U_b > 0.15$ were examined. As shown in Table 2, the relative upwelling volumes and the rankings of the four configurations vary with the threshold. A75 exhibits the largest upwelling volume at thresholds of 0.05 and

0.10, whereas A85 ranks first at 0.15. Nevertheless, the upwelling volume of A75 remains consistently greater than that of A90, with relative increases of 6.7%, 9.3%, and 12.1% at the three thresholds, respectively. These results indicate that the complete ranking is sensitive to the threshold selection, while the increase in upwelling volume for A75 relative to A90 remains consistent across the investigated thresholds.

The present results were obtained at $Re \approx 10^4$, whereas prototype-scale ARs generally operate at higher Reynolds numbers owing to their larger dimensions and different flow conditions. Previous studies of bluff-body flows have shown that flow separation from sharp-edged structures is largely governed by geometry, suggesting that the influence of frame tapering on the overall wake organisation may persist at higher Reynolds numbers [45]. Nevertheless, increasing the Reynolds number can modify boundary-layer development, shear-layer dynamics, and turbulent wake characteristics [46]. Therefore, although the present results demonstrate the effects of side-frame slope angle on recirculation dimensions, turbulence characteristics, and upwelling and wake volumes at $Re \approx 10^4$, the persistence of these trends and their quantitative magnitudes at prototype scales remains to be established.

## 4. Conclusions

This study combined laboratory measurements and large-eddy simulations (LESs) to investigate the influence of frame tapering on the hydrodynamic characteristics of open-frame artificial reefs. Four configurations with side-frame slope angles of $\theta = 90°$, 85°, 80°, and 75° (A90, A85, A80, and A75) were examined. The LES predictions showed good agreement with the experimental measurements of time-averaged streamwise velocity. The effects of frame tapering on mean flow separation, turbulent kinetic energy, instantaneous vortical structures, and upwelling and wake regions were subsequently evaluated. The main findings are summarised as follows:

(1) Frame tapering modifies the local flow separation and reattachment characteristics, thereby altering the mean wake structure, with the upper and lower recirculation regions exhibiting different responses to changes in slope angle. The upper recirculation region expands markedly as the angle decreases, with its streamwise length and maximum vertical thickness for A75 reaching approximately 2.8 and 2.5 times those of A90, respectively. By comparison, the lower recirculation region exhibits more moderate changes, with its streamwise length increasing from approximately $0.48D$ for A90 to $0.60D$ for A80 and A75.

(2) Elevated turbulent kinetic energy is mainly distributed along the separated shear layers originating from the frame members. Decreasing the slope angle modifies the spatial distribution of TKE, with more pronounced localised high-TKE regions developing near the upper separated shear layer for A80 and A75. These variations correspond to changes in the mean recirculation patterns, indicating that frame geometry influences the organisation of turbulent fluctuations within the wake.

(3) The instantaneous flow around the AR is characterised by complex three-dimensional vortical structures associated with flow separation from the frame members and interactions between streams passing through the internal openings. The $Q$-criterion visualisations reveal that the spatial distribution of these structures changes with the slope angle. In particular, the denser vortical structures become more concentrated within the main wake region for A80 and A75, with relatively fewer isolated structures extending laterally away from the wake.

(4) Frame tapering produces contrasting changes in the volumes of the upwelling and wake regions. At the reference threshold of $W_m/U_b > 0.1$, all tapered configurations exhibit larger upwelling volumes than A90, although the variation is not monotonic.

At this threshold, A75 produces the largest upwelling volume, approximately 9.3% greater than that of A90. Threshold sensitivity analysis further shows that the relative increase for A75 over A90 remains consistent across the investigated thresholds (0.05–0.15), although the rankings of the four configurations vary. In contrast, the wake volume, defined by $U_m < 0$, decreases consistently with decreasing slope angle, reaching a reduction of approximately 13.4% for A75 relative to A90.

The present study focused on a single AR under a fixed inflow velocity ($Re \approx 10^4$) and smooth-bed conditions, with the free surface represented by a rigid-lid approximation. Further investigations considering higher Reynolds numbers, different bed roughness conditions, multiple AR arrangements, and more realistic marine environments are needed to assess the robustness of the observed hydrodynamic trends and support practical reef design.

**Author Contributions:** Conceptualization, J.S. and Y.L.; methodology, J.S. and Q.X.; software, J.S.; validation, J.S. and Q.X.; formal analysis, J.S., Z.D. and D.G.; investigation, J.S. and D.G.; data curation, J.S. and D.G.; writing—original draft preparation, J.S.; writing—review and editing, J.S., Q.X., D.G., Y.L., Z.D., X.L. and L.G.; visualization, J.S. and D.G.; supervision, Y.L.; project administration, Y.L. All authors have read and agreed to the published version of the manuscript.

**Funding:** The Independent Innovation Funding Project of Changjiang Survey and Planning Design Research Co., Ltd. (CX2022Z05-1), and the Key Area Basic Research Funding of Central-level Public Welfare Scientific Research Institute (Y220011, Y224006).

**Data Availability Statement:** The raw data supporting the conclusions of this article will be made available by the authors on request.

**Acknowledgments:** The authors gratefully acknowledge the support from the funding listed above. We also appreciate anonymous reviewers who gave comments to revise the paper.

**Conflicts of Interest:** Author Qinghua Xiao was employed by Changjiang Institute of Survey, Design and Research; author Dongdong Guo was employed by Yunhe (Henan) Information Technology Co., Ltd.; and author Xiang Liang was employed by Nantong Water Conservancy Survey and Design Institute Co., Ltd. The authors declare that this study received funding from the Changjiang Survey and Planning Design Research Co., Ltd. The funder was not involved in the study design, collection, analysis, interpretation of data, the writing of this article, or the decision to submit it for publication.

## References

1. Pickering, H.; Whitmarsh, D. Artificial reefs and fisheries exploitation: A review of the 'attraction versus production' debate, the influence of design and its significance for policy. *Fish. Res.* **1997**, *31*, 39–59. [CrossRef]
2. Baine, M. Artificial reefs: a review of their design, application, management and performance. *Ocean. Coast. Manag.* **2001**, *44*, 241–259. [CrossRef]
3. Jayanthi, M.; Patterson Edward, J.K.; Malleshappa, H.; Gladwin Gnana Asir, N.; Mathews, G.; Diraviya Raj, K.; Bilgi, D.S.; Ashok Kumar, T.K.; Sannasiraj, S.A. Perforated trapezoidal artificial reefs can augment the benefits of restoration of an island and its marine ecosystem. *Restor. Ecol.* **2020**, *28*, 233–243. [CrossRef]
4. Cavallaro, M.C.; Schumann, D.A. Utility of artificial river reef structures to enhance fish habitat below a hydropeaking dam. *River Res. Appl.* **2025**, *41*, 531–538. [CrossRef]
5. Guo, D.; Zhou, L.; Wang, G.; Lai, H.; Bi, S.; Chen, X.; Zhao, X.; Liu, S.; Luo, Y.; Li, G. Use of artificial structures to enhance fish diversity in the Youjiang River, a dammed river of the Pearl River in China. *Ecol. Evol.* **2020**, *10*, 13439–13450. [CrossRef] [PubMed]
6. Zhang, J.; Zhu, L.; Liang, Z.; Sun, L.; Nie, Z.; Wang, J.; Xie, W.; Jiang, Z. Numerical study of efficiency indices to evaluate the effect of layout mode of artificial reef unit on flow field. *J. Mar. Sci. Eng.* **2021**, *9*, 770. [CrossRef]
7. Kim, D.; Woo, J.; Yoon, H.S.; Na, W.B. Wake lengths and structural responses of Korean general artificial reefs. *Ocean. Eng.* **2014**, *92*, 83–91. [CrossRef]
8. Kim, D.; Woo, J.; Yoon, H.S.; Na, W.B. Efficiency, tranquillity and stability indices to evaluate performance in the artificial reef wake region. *Ocean. Eng.* **2016**, *122*, 253–261. [CrossRef]

9. Falcão, M.; Santos, M.N.; Drago, T.; Serpa, D.; Monteiro, C.C. Effect of artificial reefs (southern Portugal) on sediment–water transport of nutrients: Importance of the hydrodynamic regime. *Estuar. Coast. Shelf Sci.* **2009**, *83*, 451–459. [CrossRef]
10. Shu, A.; Rubinato, M.; Qin, J.; Zhu, J.; Sun, T.; Yang, W.; Wang, M.; Zhang, Z. The hydrodynamic characteristics induced by multiple layouts of typical artificial M-type reefs with sea currents typical of Liaodong Bay, Bohai Sea. *J. Mar. Sci. Eng.* **2021**, *9*, 1155. [CrossRef]
11. Zheng, Y.; Kuang, C.; Zhang, J.; Gu, J.; Chen, K.; Liu, X. Current and turbulence characteristics of perforated box-type artificial reefs in a constant water depth. *Ocean. Eng.* **2022**, *244*, 110359. [CrossRef]
12. Dai, J.; Xu, Q.; Gong, Y.; Lu, Y.; Liu, X.; Mao, J. An LES Investigation of Flow Field Around the Cuboid Artificial Reef at Different Angles of Attack. *J. Mar. Sci. Eng.* **2025**, *13*, 463. [CrossRef]
13. Liu, T.L.; Su, D.T. Numerical analysis of the influence of reef arrangements on artificial reef flow fields. *Ocean. Eng.* **2013**, *74*, 81–89. [CrossRef]
14. Maslov, D.; Pereira, E.; Duarte, D.; Miranda, T.; Ferreira, V.; Tieppo, M.; Cruz, F.; Johnson, J. Numerical analysis of the flow field and cross section design implications in a multifunctional artificial reef. *Ocean. Eng.* **2023**, *272*, 113817. [CrossRef]
15. Zhou, P.; Gao, Y.; Zheng, S. Three-dimensional numerical simulation on flow behavior behind trapezoidal artificial reefs. *Ocean. Eng.* **2022**, *266*, 112899. [CrossRef]
16. Jiang, Z.; Liang, Z.; Zhu, L.; Liu, Y. Numerical simulation of effect of guide plate on flow field of artificial reef. *Ocean. Eng.* **2016**, *116*, 236–241. [CrossRef]
17. Kim, D.; Jung, S.; Na, W.B. Evaluation of turbulence models for estimating the wake region of artificial reefs using particle image velocimetry and computational fluid dynamics. *Ocean. Eng.* **2021**, *223*, 108673. [CrossRef]
18. Stoesser, T. Calculation and Eduction of Coherent Flow Structures in Open-Channel Flow Using Large-Eddy Simulations. In *Coherent Flow Structures at Earth's Surface*; Wiley: Hoboken, NJ, USA, 2013. [CrossRef]
19. Gong, Y.; Stoesser, T.; Mao, J.; McSherry, R. LES of Flow Through and Around a Finite Patch of Thin Plates. *Water Resour. Res.* **2019**, *55*, 7587–7605. [CrossRef]
20. Dai, J.; Mao, J.; Gong, Y.; Gao, H. Effect of Triangular Baffle Designs on Flow Dynamics and Sediment Transport within Standard Box Culverts. *J. Hydrodyn.* **2024**, *36*, 1142–1154. [CrossRef]
21. Gong, Y.; Xu, Y.; Mao, J.; Dai, J.; He, L.; Zhang, H.; Xu, Q. Large-Eddy Simulation of Flows Past an Isolated Lateral Semi-Circular Cavity. *J. Mar. Sci. Eng.* **2025**, *13*, 859. [CrossRef]
22. Dai, J.; Gong, Y.; Wang, K.; Gao, H.; Mao, J. Wake Dynamics and Turbulence Structures of Flow Past Two Tandem Circular Cylinders Near a Plane Wall. *Ocean. Eng.* **2025**, *334*, 121575. [CrossRef]
23. Leftheriotis, G.A.; Sibetheros, I.A.; Dimas, A.A. Large-eddy simulation of the turbulent oscillatory flow around an artificial reef. *Ocean. Eng.* **2025**, *318*, 120142. [CrossRef]
24. Weymouth, G.D.; Font, B. WaterLily.jl: A Differentiable and Backend-Agnostic Julia Solver for Incompressible Viscous Flow around Dynamic Bodies. *Comput. Phys. Commun.* **2025**, *315*, 109748. [CrossRef]
25. Smagorinsky, J. General Circulation Experiments with the Primitive Equations. I. The Basic Experiment. *Mon. Weather. Rev.* **1963**, *91*, 99–164. [CrossRef]
26. Lilly, D.K. The Representation of Small-Scale Turbulence in Numerical Simulation Experiments. In *Proceedings of the IBM Scientific Computing Symposium on Environmental Sciences*; IBM T.J. Watson Research Center: Yorktown Heights, NY, USA, 1967; pp. 195–210.
27. Yan, Z.; Chen, R.; Cai, X.C. Large eddy simulation of the wind flow in a realistic full-scale urban community with a scalable parallel algorithm. *Comput. Phys. Commun.* **2022**, *270*, 108170. [CrossRef]
28. Cho, C.; Park, J.; Choi, H. A recursive neural-network-based subgrid-scale model for large eddy simulation: Application to homogeneous isotropic turbulence. *J. Fluid Mech.* **2024**, *1000*, A76. [CrossRef]
29. Leonard, B.P. A Stable and Accurate Convective Modelling Procedure Based on Quadratic Upstream Interpolation. *Comput. Methods Appl. Mech. Eng.* **1979**, *19*, 59–98. [CrossRef]
30. Weymouth, G.D.; Yue, D.K.P. Boundary Data Immersion Method for Cartesian-Grid Simulations of Fluid-Body Interaction Problems. *J. Comput. Phys.* **2011**, *230*, 6233–6247. [CrossRef]
31. Maertens, A.P.; Weymouth, G.D. Accurate Cartesian-Grid Simulations of Near-Body Flows at Intermediate Reynolds Numbers. *Comput. Methods Appl. Mech. Eng.* **2015**, *283*, 106–129. [CrossRef]
32. Kara, S.; Kara, M.C.; Stoesser, T.; Sturm, T.W. Free-Surface versus Rigid-Lid LES Computations for Bridge-Abutment Flow. *J. Hydraul. Eng.* **2015**, *141*, 04015019. [CrossRef]
33. Khosronejad, A.; Ghazian Arabi, M.; Angelidis, D.; Bagherizadeh, E.; Flora, K.; Farhadzadeh, A. Comparative Hydrodynamic Study of Rigid-Lid and Level-Set Methods for LES of Open-Channel Flow. *J. Hydraul. Eng.* **2019**, *145*, 04018077. [CrossRef]
34. Ouro, P.; Wilson, C.A.M.E.; Evans, P.; Angeloudis, A. Large-eddy simulation of shallow turbulent wakes behind a conical island. *Phys. Fluids* **2017**, *29*, 126601. [CrossRef]
35. Fröhlich, J.; Mellen, C.P.; Rodi, W.; Temmerman, L.; Leschziner, M.A. Highly resolved large-eddy simulation of separated flow in a channel with streamwise periodic constrictions. *J. Fluid Mech.* **2005**, *526*, 19–66. [CrossRef]

36. Stoesser, T. Large-eddy simulation in hydraulics: Quo Vadis? *J. Hydraul. Res.* **2014**, *52*, 441–452. [CrossRef]
37. Hunt, J.C.R.; Wray, A.A.; Moin, P. Eddies, streams, and convergence zones in turbulent flows. In *Studying Turbulence Using Numerical Simulation Databases, 2: Proceedings of the 1988 Summer Program*; Center for Turbulence Research, Stanford University: Stanford, CA, USA, 1988; pp. 193–208.
38. Dai, J.; Liao, P.; Hu, Y.; Wang, K.; Jin, C.; Yang, R.; Gong, Y.; Mao, J. Turbulent flow around a sidewall triangular baffle in a culvert under varying baffle orientations. *Phys. Fluids* **2025**, *37*, 115151. [CrossRef]
39. Dai, J.; Luo, Q.; Stoesser, T.; Gong, Y.; Mao, J. Turbulent free-surface flow through an idealised nature-like fish pass. *Eng. Appl. Comput. Fluid Mech.* **2026**, *20*, 2735739. [CrossRef]
40. Yan, G.; Yuan, S.; Dai, J.; Liao, P.; Sun, J.; Tang, Z.; Tang, H. Turbulent flow at confluences under different tributary floodplain topographies. *Phys. Fluids* **2026**, *38*, 065120. [CrossRef]
41. Sadeque, M.; Rajaratnam, N.; Loewen, M. Effects of bed roughness on flow around bed-mounted cylinders in open channels. *J. Eng. Mech.* **2009**, *135*, 100–110. [CrossRef]
42. Liu, Y.; Stoesser, T.; Fang, H.; Papanicolaou, A.; Tsakiris, A.G. Turbulent flow over an array of boulders placed on a rough, permeable bed. *Comput. Fluids* **2017**, *158*, 120–132. [CrossRef]
43. Jiao, L.; Zheng, Y.x.; Gong, P.h.; Guan, C.t. Numerical simulation and PIV experimental study of the effect of flow fields around tube artificial reefs. *Ocean. Eng.* **2017**, *134*, 96–104. [CrossRef]
44. Wang, X.; Liu, X.; Tang, Y.; Zhao, F.; Luo, Y. Numerical Analysis of the Flow Effect of the Menger-Type Artificial Reefs with Different Void Space Complexity Indices. *Symmetry* **2021**, *13*, 1040. [CrossRef]
45. Derakhshandeh, J.F.; Alam, M.M. A review of bluff body wakes. *Ocean. Eng.* **2019**, *182*, 475–488. [CrossRef]
46. Schewe, G. Reynolds-number effects in flow around more-or-less bluff bodies. *J. Wind. Eng. Ind. Aerodyn.* **2001**, *89*, 1267–1289. [CrossRef]


**Disclaimer/Publisher's Note:** The statements, opinions and data contained in all publications are solely those of the individual author(s) and contributor(s) and not of MDPI and/or the editor(s). MDPI and/or the editor(s) disclaim responsibility for any injury to people or property resulting from any ideas, methods, instructions or products referred to in the content.